


RESEARCH

Open Access



# Deep tissue super-resolution imaging with adaptive optical two-photon multifocal structured illumination microscopy

Chenshuang Zhang<sup>1</sup>, Bin Yu<sup>1\*</sup>, Fangrui Lin<sup>1</sup>, Soham Samanta<sup>1</sup>, Huanhuan Yu<sup>1</sup>, Wei Zhang<sup>2</sup>, Yingying Jing<sup>1</sup>, Chunfeng Shang<sup>3,4</sup>, Danying Lin<sup>1\*</sup>, Ke Si<sup>5</sup>, Wei Gong<sup>5</sup> and Junle Qu<sup>1\*</sup> 

\*Correspondence:  
yubin@szu.edu.cn; dylin@szu.edu.cn; jlqu@szu.edu.cn

<sup>1</sup> Key Laboratory of Optoelectronic Devices and Systems of Ministry of Education and Guangdong Province, College of Physics and Optoelectronic Engineering, Shenzhen University, Shenzhen 518060, China

<sup>2</sup> Department of Computer Science and Technology, Anhui University of Finance and Economics, Bengbu 233030, China

<sup>3</sup> Guangdong-Hongkong-Macau Institute of CNS Regeneration, Ministry of Education CNS Regeneration Collaborative Joint Laboratory, Jinan University, Guangzhou 510632, China

<sup>4</sup> Shenzhen Institute of Neuroscience, Shenzhen 518057, China

<sup>5</sup> MOE Frontier Science Center for Brain Science & Brain-Machine Integration, NHC and CAMS Key Laboratory of Medical Neurobiology, School of Brain Science and Brain Medicine, Zhejiang University, Hangzhou 310058, China

## Abstract

Visualization of axons and dendritic spines is crucial in neuroscience research. However, traditional microscopy is limited by diffraction-limited resolution and shallow imaging depth, making it difficult to study neuronal dynamics. Two-photon multifocal structured illumination microscopy (2P-MSIM) provides super-resolution imaging along with a reasonably good penetration, but it is vulnerable to optical aberrations in deep tissues. Herein we present a novel non-inertial scanning 2P-MSIM system incorporated with adaptive optics (AO) which allows for super-resolution imaging with effective aberration correction. Our strategy is designed to correct both laser and fluorescence paths simultaneously using a spatial light modulator and a deformable mirror respectively, providing better results than the individual path corrections. The successful implementation of adaptive optical two-photon multifocal structured illumination microscopy (AO 2P-MSIM) has allowed for the super-resolution imaging of neuronal structures in a mouse brain slice at great depths and dynamic morphological characteristics of zebrafish motoneurons in vivo.

**Keywords:** Super-resolution, Adaptive optics, In vivo imaging, Neurons

## Introduction

Neurons, the fundamental units of the nervous system, are constantly engaged in diverse computations through their delicate dendritic and axonal processes [1]. The shape of the dendritic spines has a great influence on synaptic computation, and their morphological changes are frequently observed during synaptic plasticity [2, 3]. Optical microscopy has long been an indispensable tool for visualizing neuronal structures and functions [4–6], but traditional imaging systems with their limited resolution and imaging depth are insufficient for detailed visualization of various synaptic spines and in vivo morphological changes of neurons. The emergence of two-photon excitation microscopy (2PEM) has provided significant benefits for in vivo imaging, such as inherent optical sectioning, reduced photodamage to living samples, and deeper penetration into thick tissues [7, 8]. To improve the imaging resolution beyond the diffraction limit, 2PEM was subsequently combined

with structured illumination microscopy, leading to the development of new hybrid microscopic techniques such as two-photon multifocal structured illumination microscopy (2P-MSIM) [9] and two-photon instant structured illumination microscopy (2P-ISIM) [10, 11]. Generally, these techniques follow the principle of image scanning microscopy (ISM) that combines the resolving ability of a pinhole with the fast detection aptitude of widefield imaging [12, 13], making it beneficial for imaging deep tissues such as *Caenorhabditis* and mouse liver tissue [9]. A microlens array is often used to generate the two-photon focus array. Although this strategy with low energy consumption and good uniformity can endure the use of the high-energy laser beam, the number of foci and the distance between foci are unaltered once the microlens array is integrated into the system. Moreover, obtaining super-resolution images in deep tissues using 2P-MSIM can pose challenges due to multiple scattering and aberrations, which can degrade the imaging depth and spatial resolution.

Adaptive optics (AO) is an effective method to recover spatial resolution and signal-to-noise ratio (SNR) in deep tissues and complex environments [14–20]. This is particularly important in two-photon super-resolution microscopy studies where increasing imaging depth leads to optical aberrations caused by tissue heterogeneities and differences in refractive index. Therefore, correcting optical aberrations that adversely impact both the image quality as well as the resolution using AO can surpass the hurdle of studying neuronal processes and synapses in the subcellular context with fine-structural details. Generally, a deformable mirror (DM) or a spatial light modulator (SLM) is placed in the excitation path to recover the focal volume and peak intensity [21, 22]. The reflecting surface of DM is a continuous membrane controlled by a few actuators that can correct the relatively low-order aberrations and avoid loss of energy induced by diffraction effects from segments. The SLM, another widely used AO corrector in the excitation path, uses aligned nematic crystals to correct aberrations but has limitations with regard to polarized light and wavelength sensitivity. Additionally, AO correction in the emission path is also indispensable for obtaining super-resolution images in deep tissues [11].

In this work, we developed a novel adaptive optical two-photon multifocal structured illumination microscopy (AO 2P-MSIM) system for high-quality super-resolution imaging, introducing AO for the first time into 2P-MSIM. The system differs from conventional methods by incorporating a single high-speed SLM instead of a microlens array and galvanometer scanners, offering greater flexibility in generating and shifting focus arrays (e.g., a single focus scanning for AO correction and a focal array scanning for super-resolution imaging). The SLM also facilitates the correction of laser path aberrations ensuring that the focal shape and peak intensity are maintained in deep tissues. Moreover, to further improve the AO correction efficiency during the acquisition of super-resolution images, a DM was placed in the fluorescence path so that the aberration-contaminated signals, adversely impacting the attainable resolution can be reverted. Eventually, the judiciously constructed AO 2P-MSIM system with super-resolution imaging and optical sectioning credentials was successfully applied not only to observe neurons in mouse brain slices with nanoscale resolution but also to demonstrate the nanoscale neuronal dynamics in living zebrafish larvae.

## Results

### AO 2P-MSIM system

A rationally constructed AO 2P-MSIM system was set up for super-resolution imaging studies (Fig. 1). In the aberration detection process (purple rectangle), a flip mirror was aptly placed to divert fluorescence emission to a Shack–Hartmann wavefront sensor (SHS). The SLM loaded phase pattern was instrumental in generating a single focus within the specimen and the related aberration wavefront was detected by the SHS, while the fluorescence emission was directed by the DM (working as a flat mirror). For 2P-MSIM imaging with AO correction (green rectangle), a corrective phase pattern was superposed with a pre-designed phase pattern for a multifocal array to generate the AO-corrected laser focus array. Meanwhile, the DM loaded corrective voltages compensated the aberrations in the fluorescence path. Finally, the AO-corrected images of 2P-MSIM were captured by an electron multiplying charge-coupled device (EMCCD).

In order to make the system design more compact and to overcome the artifacts caused by the mechanical inertia of galvanometer scanners, the shifting of focus arrays was controlled in such a way that it could cover the full field of view (Figure S1). To correct aberrations with AO, the fluorescence signal of two-photon excitation was considered as a nonlinear guide star [21, 23], since two-photon excitation usually occurs only within a very small area around the focus. Once the aberrations were estimated from the detected wavefront by the SHS, the corrective phase pattern and voltages were applied to the SLM and DM simultaneously to correct the aberrations in the laser and fluorescence paths, respectively. It is worth mentioning here that before measuring and correcting sample-induced aberrations, the imaging system must be calibrated to compensate

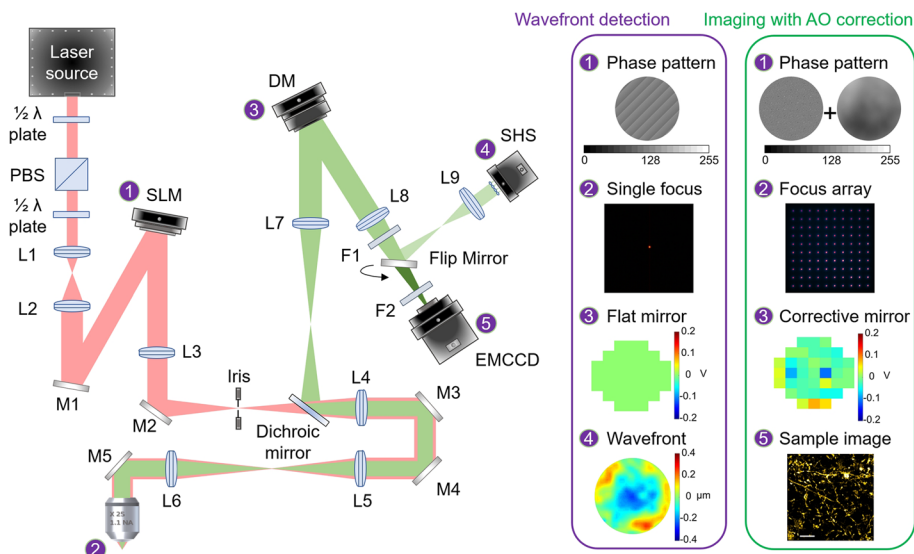


**Fig. 1** Schematic diagram of AO 2P-MSIM system. 1: SLM; 2: objective; 3: DM; 4: SHS; 5: EMCCD. The flip mirror can be switched between the EMCCD and SHS. L1–L9: lenses. F1 and F2: filters. Purple rectangle: Wavefront detection. The SLM loads phase pattern for a single focus to exciting specimen; The SHS detects aberration wavefront, while the DM is set to a flat mirror. Green rectangle: Super-resolution imaging with AO correction. The SLM loads phase patterns for an AO-corrected laser focus array; The DM loads corrective voltages to compensate for the fluorescence aberrations; The EMCCD captures corrected images. Scale bar, 5  $\mu\text{m}$

for its own aberrations. Next, yellow-green fluorescent beads (diameter 1  $\mu\text{m}$ ), placed on a coverslip surface were used to evaluate the performance of system correction (Figure S2). The shape of the guide star showed significant asymmetry without any system correction. Even though a significant improvement in the signal intensity was achieved only through the excitation path-related system correction, it was hardly useful for the betterment of shape. On the other hand, the shape of the guide star was perfectly restored with the system correction in the emission path. Therefore, it is mandatory to have system corrections in both the excitation and emission paths for attaining the optimal intensity and shape of the guide star. In this context, SLM and DM can be simultaneously used for effective AO correction. Very little aberration (as measured by SHS) was observed after the full system correction, which reiterated the robustness of the system correction.

Following the optimization of system correction, a series of raw images of the Thy1-YFP mouse brain slice were captured at 106  $\mu\text{m}$  depth (Figure S3) with and without sample correction. Widefield (WF) images with or without sample corrections (represented as Full AO WF images and Sys AO WF, respectively) were reconstructed by directly summing the corresponding raw data. Furthermore, using the multifocal structured illumination microscopy (MSIM) principle, a series of raw images were filtered, pinholed, and scaled to obtain the intermediate images (pixel reassignment) with and without sample correction (Full AO PR and Sys AO PR, respectively). Finally, by further deconvoluting PR images, the corresponding Sys AO MSIM (with system correction but no sample correction) and Full AO MSIM (with both system correction and sample correction) images were obtained. According to the comparison of intensity profiles, AO's contribution to resolution enhancement and SNR improvement provides a foundation for the next super-resolution reconstruction. To improve imaging performance, AO correction, pixel reassignment, and deconvolution all work together. As shown in Figure S4, the SNR and resolution of the pixel reassignment image are significantly higher than those of widefield images. Direct deconvolution processing has very limited resolution improvement on widefield images, and it can also produce non-negligible artifacts due to the sensitivity of deconvolution algorithms to noise. Using deconvolution algorithms on the basis of pixel reassignment can significantly improve resolution. When comparing deconvolution algorithms, the image enhancement obtained by Richardson–Lucy deconvolution (utilized in our MSIM processing) and Blind deconvolution are nearly identical. In contrast, the Wiener filter may result in unreliable improvements in image resolution due to noticeable artifacts.

We assessed the AO 2P-MSIM system by measuring the point spread functions (PSFs) in increasingly aberrated environments, using fluorescent beads with 100 nm diameter. First, the optimum resolution was estimated by imaging beads on a coverslip surface (Figure S5). With system AO correction, the shapes of the bead are almost symmetrical in both lateral and axial directions. We measured the full width at half maximum (FWHM) of the intensity profiles on the widefield images, and the mean value for 32 beads was  $349 \pm 21$  nm (lateral) and  $741 \pm 64$  nm (axial), respectively. After MSIM reconstruction, we obtained a lateral FWHM of  $142 \pm 11$  nm and an axial FWHM of  $493 \pm 41$  nm. Next, we embedded the beads in agarose and measured the system resolution at various depths within the sample (Figure S6). As anticipated, without AO correction, PSFs were enlarged both in the lateral and axial directions due to the increasing

aberrations. The average wavefronts detected at different depths (10, 100, 300, and 500  $\mu\text{m}$  from the coverslip) further revealed that if only system AO correction is done without any sample correction, it resulted in the gradual increase in aberrations with increasing depth (Figure S7). However, employing both system AO correction as well as sample AO correction concurrently demonstrated the negligible change in aberrations upon increasing depth which highlighted the improvements in AO performance. As shown in Table S1, AO correction can improve the spatial resolutions throughout the 500- $\mu\text{m}$  imaging depth. Comparing the Sys AO WF and Full AO MSIM images, it was evident that the AO 2P-MSIM system with combined aberration correction (both system and sample corrections) recovered the lateral resolution from  $423 \pm 24$  nm to  $153 \pm 9$  nm and axial resolution from  $1379 \pm 120$  to  $735 \pm 74$  nm at a 500- $\mu\text{m}$  depth. The PSFs were well restored by detecting wavefronts with SHS and reducing aberrations with both SLM and DM.

#### Application of AO 2P-MSIM in biological samples

We next implemented the AO 2P-MSIM to biological specimens wherein a fixed brain slice from a Thy1-YFP mouse was imaged (Fig. 2). Since neuron bodies possessed bright fluorescent signal, the guide star for AO correction was generated from a neuron body. Around 319  $\mu\text{m}$  below the coverslip, neurons were imaged across a total depth of 12  $\mu\text{m}$  which has been shown as the maximum intensity projection (MIP) image with depth coding (Fig. 2A). At a depth of approximately 316  $\mu\text{m}$ , the adverse effect of optical aberrations on imaging made the two-photon excitation imaging results very blurred (Fig. 2B). Widefield images with sample AO correction showed blurry but detectable dendritic structures (Fig. 2B, middle). However, AO correction (for sample-induced aberrations) followed by the MSIM reconstruction resulted in easily detectable high-resolution dendritic structures (e.g., dendrite and dendritic spines, white arrows) (Fig. 2B, bottom). In contrast to the widefield images that showed uniform strips, the fine structure of dendrites was clearly visualized using aberration-corrected 2P-MSIM, as previously reported [24, 25]. Subsequently, the improvements in spatial resolution were characterized through the quantification of spatial frequency space (Fig. 2C). Compared to the widefield images with approximately 300 nm resolution, the sample AO correction being coupled with MSIM reconstruction provided a spatial resolution as high as approximately 150 nm, which was instrumental in resolving the fine dendritic structural features. As shown in Fig. 2D, dendritic spines and spine necks (white arrows) can be clearly observed from the Full AO MSIM images, but not from the widefield images. The corresponding intensity profiles are shown as the yellow (Sys AO WF), blue (Full AO WF), and red (Full AO MSIM) lines (Fig. 2E). Spine heads and spine necks were effectively sharpened by the combined effect of AO correction and MSIM reconstruction (approximately 144 nm of spine neck). The wavefronts without and with AO correction for sample-induced aberrations demonstrated that AO correction could certainly reduce aberrations in deep tissues (Fig. 2F). It should be noted that because complex in-situ aberrations exist at every single position, the average correction can only moderately compensate for field of view aberrations. However, it was still capable of significantly improving the results. This is a grudging compromise between imaging speed and correction accuracy. We further characterized the detailed structure of the neurons by

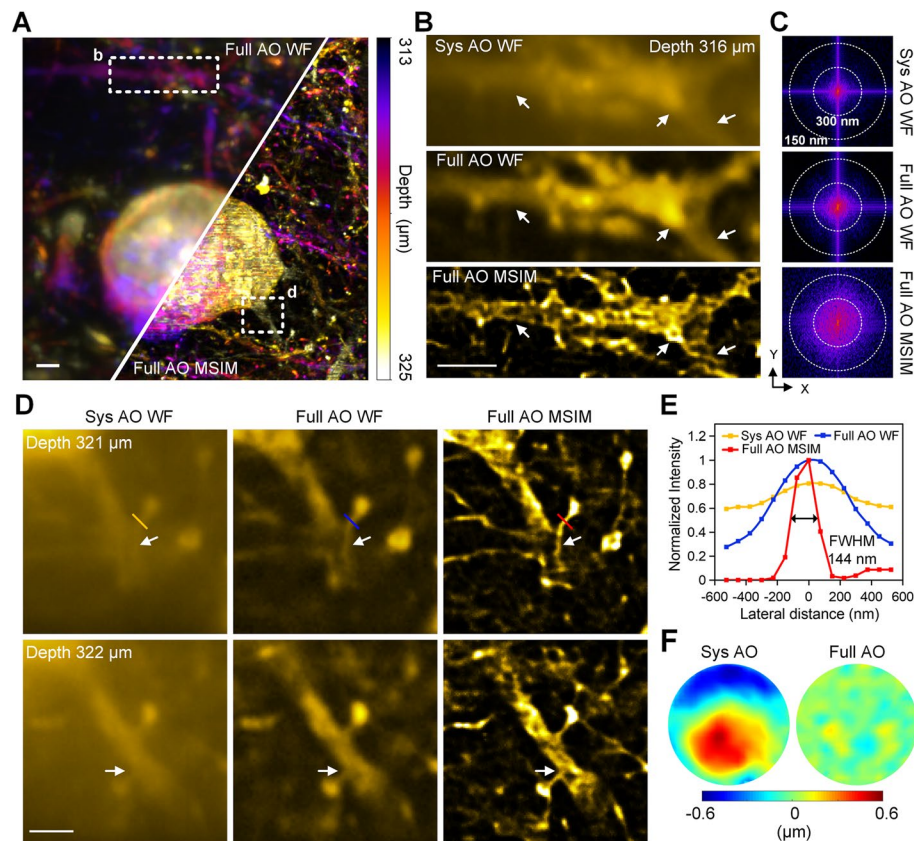


**Fig. 2** AO 2P-MSIM improves spatial resolution in a brain slice. AO 2P-MSIM imaging in a Thy1-YFP brain slice at 325–313- $\mu\text{m}$  depth. **A** Maximum intensity projection (MIP) of full AO WF and full AO MSIM image stacks (1- $\mu\text{m}$  Z step). **B** Higher magnification views of the top boxed region in **(A)** at 316- $\mu\text{m}$  depth are shown. Sys AO WF and Full AO WF indicate widefield images without and with sample AO correction, respectively, and Full AO MSIM indicates the MSIM reconstructed image with sample AO correction. White arrows indicate obvious resolution improvement. **C** Lateral resolution improvement after AO correction and MSIM reconstruction is quantified in spatial frequency space. **D** Higher magnification views of the bottom boxed region in **(A)** at 321  $\mu\text{m}$  and 322  $\mu\text{m}$  are shown. White arrows indicate the dendritic spines. **E** Line profiles across the dendritic spine neck corresponding to **(D)**. The signal was normalized to the AO condition (0 to the maximum intensity of the Full AO WF image). **F** Wavefronts detected by SHS before and after sample AO correction are shown. Scale bar, 2  $\mu\text{m}$

super-resolution imaging with full AO correction (Figure S8). Visualization of various branched and unbranched dendritic spines using AO 2P-MSIM system also opened up the possibility of deciphering their individual roles in dendritic computations [25, 26].

While the signal of endogenous fluorophores may not be strong enough for wavefront detection by SHS, additional fluorophores or dyes can be expressed or loaded as guide stars to improve the imaging depth [11, 23]. We adopted this approach on living zebrafish larvae of 5 days post fertilization (dpf) (Fig. 2). The map of the imaging location is shown in Figure S9A. Essentially, the zebrafish larvae (mnx1: mGFP) were labeled with a bright cell-permeable fluorescent dye CellTracker Red to enable the effective wavefront measurement at 183  $\mu\text{m}$  depth. Therefore, it was possible to track the wavefront measurement during the in vivo AO 2P-MSIM imaging of the zebrafish larvae motoneurons expressing mGFP. The AO 2P-MSIM images, where both the sample-induced aberrations and the system-induced aberrations were corrected through AO (denoted

as Full AO MSIM), revealed significant improvements in the resolution and signal intensity than the widefield images either with only system AO correction or both system and sample AO corrections (Fig. 2A). The reconstruction of the AO 2P-MSIM images with both sample AO correction as well as system AO correction was able to resolve the super-resolution fine structures of an intertwined axonal network within the spinal cord (Fig. 3B). The Full AO MSIM image was able to provide the optical sectioning and desired resolution for studying the neural structures, as confirmed by the intensity profiles (Fig. 3C). The apparent improvements in imaging quality were shown in Fig. 3D, wherein a ring structure rather than a spherical structure can be clearly identified upon full (system + sample) AO correction followed by MSIM processing. We pre-measured the aberrations of the field of view and evaluated the effect of sample AO correction on compensating the average aberrations (Fig. 3E). Furthermore, we also observed that the sample AO correction in combination with MSIM reconstruction can provide a clearer view of the extended axons of spinal motoneurons (Figure S9B).

Axons, extending to form the synaptic contacts, play a crucial part in establishing circuits for the development of neuronal networks [27, 28]. It is critical, yet difficult, to track the fine structural changes in the neuronal networks during synapse formation in order to understand how the thin filopodia can lead the axonal process [6]. As shown in Figure S10, the distribution of motor neurons is very rich in the connection between

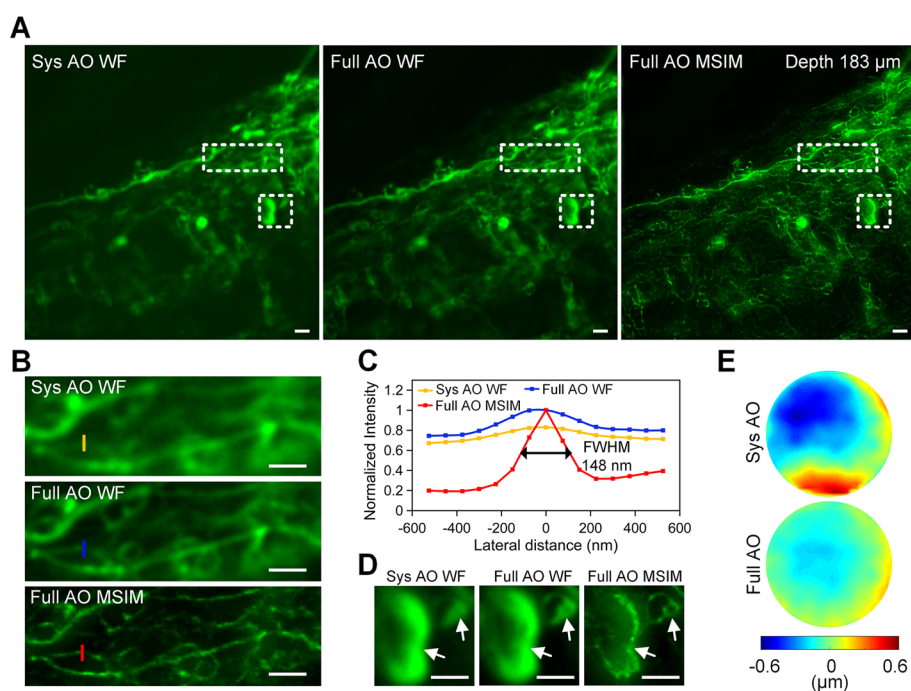


**Fig. 3** AO 2P-MSIM imaging of dense motoneurons in living *mnx1:mGFP* zebrafish. In vivo AO 2P-MSIM imaging of dense *mnx1:mGFP* zebrafish motoneurons in the spinal cord. **A** Sys AO WF, Full AO WF, and Full AO MSIM images in the same field of view. The signal from the Sys AO WF image was artificially increased (2-fold) for better visualization. **B** Higher magnification views of the top boxed region in (A) are shown. **C** Line profiles across an axonal structure corresponding to (B). **D** Higher magnification views of the bottom boxed region in (A) are shown. White arrows indicate a ring structure revealed with significant resolution improvement after sample-induced AO correction and MSIM reconstruction. **E** Wavefronts before and after sample correction are shown. Scale bar, 2  $\mu\text{m}$

the brain and the spinal cord. Neurons were imaged at different depths from the surface of zebrafish and the obtained widefield and super-resolution images with full AO correction were compared (Figure S10B). The FWHM, calculated at 332  $\mu\text{m}$  depth for the filopodia of a neuron was about 154 nm. This *in vivo* AO 2P-MSIM imaging was also effectively employed to visualize the delicate structure and dynamic changes of the motoneurons in 2-dpf-old zebrafish larvae for approximately 120 min (Fig. 4). Motoneurons at 210–230  $\mu\text{m}$  depth were observed by using time-lapse diffraction-limited widefield imaging with/without sample-induced AO correction and MSIM reconstruction (Fig. 4A). Moreover, the improvement in spatial resolution gained through the combined effect of aberration corrections and MSIM processing was also confirmed by the recovery of spatial frequency components as shown in the spatial frequency space (Fig. 4B), which enabled the scope of resolving fine structures of the zebrafish motoneurons underneath the skin at 218  $\mu\text{m}$  depth. To further illustrate the combined effect of AO-mediated correction and MSIM reconstruction on the imaging quality, a portion of Fig. 4A, marked with purple arrows (showing a protrusion on the axon) was magnified.

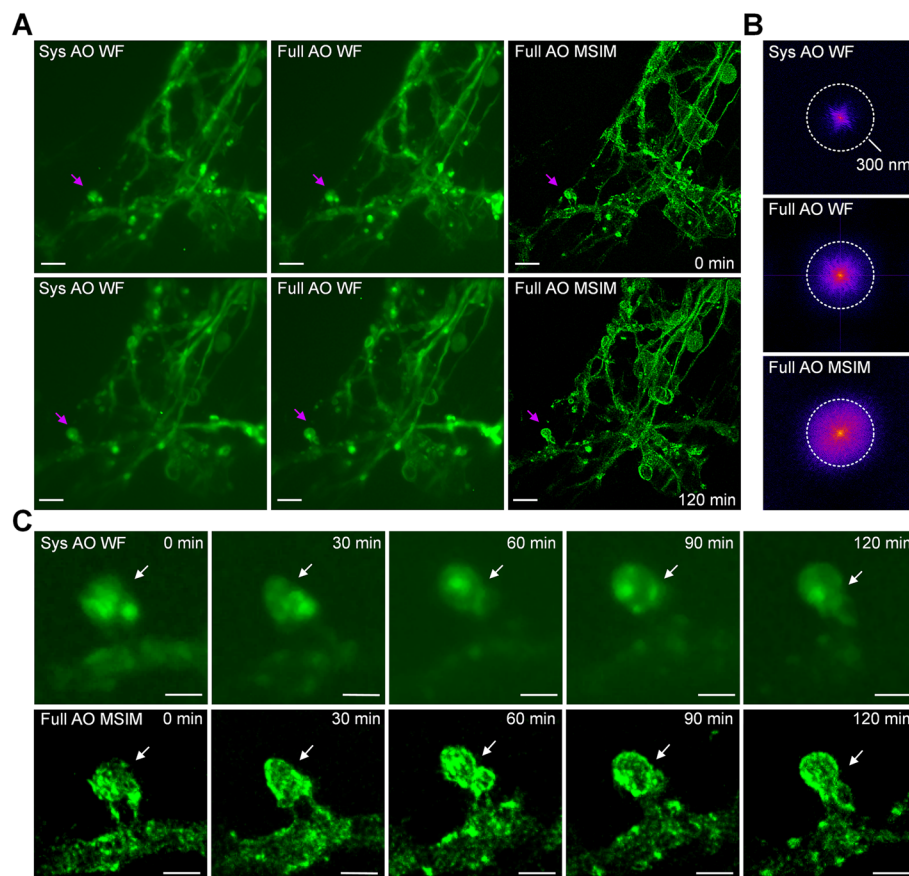


**Fig. 4** Time-lapse AO 2P-MSIM imaging of motoneurons extended from the spinal cord. Time-lapse AO 2P-MSIM imaging of *mnx1:mGFP* zebrafish motoneurons extended from the spinal cord at 210–230- $\mu\text{m}$  depth. **A** Representative MIPs of the Sys AO WF, Full AO WF, and Full AO MSIM images. Arrows point to highly dynamic structures. Scale bar, 5  $\mu\text{m}$ . **B** Lateral resolution improvement by AO correction and MSIM reconstruction is quantified in spatial frequency space calculated from images of the motoneurons at 218- $\mu\text{m}$  depth (0 min). **C** Higher magnification views of time-lapse AO off WF and AO on MSIM images for the region pointed by purple arrows in (A). Scale bar, 2  $\mu\text{m}$



The magnified views of the selected area suggested that compared to the blurry widefield images (Fig. 4C, top) the judiciously constructed AO 2P-MSIM system can provide the scope of much clearer visualization of the in vivo neuronal dynamics (Fig. 4C, bottom) and hence, the system can be successfully employed to monitor the dynamic morphological changes of the selected protrusion on the axon. Especially, the delicate structural components connecting the protrusion with the axon were conspicuous when AO 2P-MSIM was implemented which was not visible with the Sys AO WF and Full AO WF images. Additionally, to assess the improvement of axial resolution in biological specimens, AO 2P-MSIM was utilized to image mitochondria in zebrafish larvae expressing EGFP (Figure S11). The results showed a lateral resolution of 163 nm and an axial resolution of 783 nm at a depth of 300  $\mu\text{m}$ .

## Discussion

To expedite the super-resolution imaging in deep tissues, the rationally designed AO 2P-MSIM method mainly worked on combining the following three aspects: (1) improving the signal recovery ability through AO correction for the system- and sample-induced aberrations; (2) upholding the super-resolution imaging credential of MSIM; and (3) enabling the deep penetrating capacity of two-photon excitation. Although MSIM cannot achieve the ultra-high spatial resolution akin to stimulated emission depletion microscopy (STED), stochastic optical reconstruction microscopy (STORM), or photo-activated localization microscopy (PALM) due to constraint in its basic principle, the possibility of achieving super-resolution images at a deeper imaging depth makes it an excellent choice for exploring it in the nanoscopic imaging of neurons.

In the AO 2P-MSIM system, a SLM is triggered to load phase patterns in sync with electron multiplying charge-coupled device (EMCCD) frames. Multi-focal arrays traversed the entire field of view pixel by pixel during the MSIM scanning process, and the corresponding signal was recorded in a series of raw images. However, in external trigger mode, EMCCD frame rates are limited by the area size, such as  $512 \times 512$  pixels at 50 Hz and  $1024 \times 1024$  pixels at 26 Hz. Thus, in the AO 2P-MSIM system,  $512 \times 512$  pixels were used, and the imaging area of the EMCCD is approximately 65  $\mu\text{m}$ . Furthermore, the field of view used in experiments is approximately 50  $\mu\text{m}$  to ensure that all fluorescence signals are collected by the EMCCD. In future, a faster and more sensitive image detector (and possibly a higher-speed SLM) can be introduced to further improve our AO 2P-MSIM system towards achieving better imaging quality while studying the neuronal dynamics with nanoscopic resolution. Deep learning can further improve the optical performance of the super-resolution microscopy, such as resolution enhancement [29] and faster acquisition speed by undersampling [30]. Furthermore, a “hybrid” synchronization of the SLM and EMCCD can be potentially used to break the limitation of EMCCD rate in imaging speed. As shown in Figure S12, multifocal arrays traverse the entire field of view according to raster-scanning. Normally, the synchronization for scanning and imaging can be achieved if both SLM and EMCCD are tuned at the same rate. In a multiplexing trigger mode, the series pattern loaded onto the SLM at  $n$ -fold rate than EMCCD. Essentially, in our 2P-MSIM system, the scanning of multi-focal arrays with SLM at a frame rate of 360 Hz enabled the image collection by EMCCD at a frame rate of 80 Hz which led to an overall imaging speed of approximately 2 s, making

the system as fast as the previously reported 2P-MSIM and 2P-ISIM systems [9, 10]. As shown in Figure S13, the multiplexing trigger mode can overcome the EMCCD rate limitation in imaging speed. It may, however, result in a decrease in image contrast. The entire field of view is scanned in one exposure cycle in 2P-ISIM. It should be noted that our 2P-MSIM is capable of recording both the fluorescence signal generated by the sample (during the excitation dwell time) and the instrument noise (during the non-dwell time) individually in separate images, allowing for easy post-processing noise reduction, whereas such noise reductions are not possible in 2P-ISIM systems. The foci in the 2P-MSIM system should be sufficiently sparse to avoid possible fluorescent crosstalk caused by parallel excitation in highly scattered or deep tissues. Sparse foci, on the other hand, necessitate a lengthy scan time to cover the entire field of view. Based on imaging depth and biological sample characteristics, it is critical to strike a balance between crosstalk and acquisition time. Furthermore, the number of laser foci is limited due to the damage threshold levels and the SLM's modulation efficiency, resulting in a limited field of view.

## Conclusions

The advanced AO 2P-MSIM system was developed by judiciously integrating SLM in the laser path and DM in the fluorescence path so that the aberrations arisen out of both the excitation as well as emission can be corrected respectively. Designing this AO-based super-resolution microscopic system with dual-path (both excitation and emission path) aberration correction aptitude revealed much better imaging performance compared to the systems enduring only SLM-mediated aberration correction in the excitation path. Moreover, the DM correction in the emission path is key to realizing super-resolution imaging in deep tissues as it can salvage the SNR and resolution from serious degeneration caused by optical aberrations. In this method, SLM has been introduced for the excitation path AO correction based on couple of important considerations. Primarily, SLM has higher correction precision than DM which can enable better realization of the corrected multifocal array in MSIM imaging. More importantly, introducing a single SLM can solve the dual purpose by simultaneously enabling both MSIM imaging and AO correction, which vouched for a more compact and flexible AO 2P-MSIM system. The possibility of achieving super-resolution images at a deeper imaging depth makes AO 2P-MSIM an excellent choice for exploring it in the super-resolution imaging of neurons.

## Methods

### Adaptive optical two-photon MSIM system set-up

The AO 2P-MSIM system (Fig. 1) mainly comprised three light paths for two-photon near-infrared (NIR) excitation (red), visible fluorescence detection (dark green), and wavefront measurement (light green). The intensity of the pulsed light from the laser source (either a 920 nm femtosecond laser (Spark Lasers, ALCOR 920) or a 1036 nm femtosecond laser (YSL, Femto YL<sup>TM</sup>)) was controlled by a  $1/2 \lambda$  wave plate (Thorlabs, AHWP05M-980) and a polarizing beam splitter (PBS) cube (Thorlabs, CCM1-PBS252). Then, the laser beam was expanded by a pair of NIR achromatic lenses (L1 and L2, focal lengths  $f_1 = 25$  mm and  $f_2 = 80$  mm, respectively) to a  $1/e^2$  diameter of 11 mm before

being reflected to a NIR-responsive high-speed phase-only spatial light modulator (SLM NIR, Meadowlark, HSP1920-1152) at  $10^\circ$ . Another  $1/2 \lambda$  wave plate (Thorlabs, AHWP05M-980) was placed between the PBS cube and the expanding lenses to facilitate the desired polarization alignment of the SLM. Another two pairs of NIR achromatic relay lenses (L3 and L4, L5 and L6,  $f_3 = 300$  mm,  $f_4 = 400$  mm,  $f_5 = 180$  mm, and  $f_6 = 300$  mm, respectively) were used to create a magnified image of the SLM at the rear pupil plane of the objective (Nikon, CFI Apo LWD 25XW, 1.1 NA and 2 mm WD). The SLM loaded the phase patterns to generate and shift a diffraction-limited focal spot/multifocal array for two-photon excitation. An iris (Thorlabs, ID25) was placed in the focal plane of L3 to filter unnecessary diffraction orders. Approximately 50% laser power was retained at the rear pupil plane of the objective.

The fluorescence signal collected by the objective was modified to a  $1/e^2$  beam diameter of 13.2 mm by relay lenses 6, 5, 4, and 7 ( $f_7 = 500$  mm), and reflected by a dichroic mirror (Thorlabs, DMLP805R) to a deformable mirror (DM, Imagine Optic, 52 actuators,  $\pm 50$ - $\mu\text{m}$  stroke, 15-mm pupil). The fluorescence beam reflected from the DM was focused by a lens (L8,  $f_8 = 600$  mm) onto an EMCCD (Andor, Life 888, 1,024 pixels  $\times$  1,024 pixels;  $13 \mu\text{m} \times 13 \mu\text{m}$ ) to obtain the image of the excited specimen. To measure the wavefront for AO correction, we diverted the fluorescence signal to the SHS (Imagine Optic, HASO3-First,  $40 \times 32$  microlenses) using a flip mirror (Thorlabs, PFR10-P01) and another achromatic lens (L9,  $f_9 = 150$  mm). Two emission filters F1 (TF1, FESH0850, Thorlabs) and F2 (ET525/50 Chroma), Table S2) were placed after L8 to isolate fluorescence before being collected on the EMCCD and the SHS.

It is worth noting that the above-mentioned pairs of relay lenses (L3 and L4; L5 and L6; L4 and L7; and L8 and L9) were placed in  $4f$  imaging configurations, thereby ensuring that the SLM, the rear pupil plane of the objective, the DM, and the SHS are conjugated.

### Single focal spot and multifocal array generation and scanning

Weighted Gerchberg-Saxton (WGS) algorithm was utilized to calculate the phase pattern loaded onto the SLM [31], generating a single focal spot or a multifocal array. The spot or array was shifted by adding a series of linear grating phases to the predetermined phase pattern (the detailed principle was shown in the Supplemental information). By changing phase patterns loaded onto the SLM sequentially, the focus or focal array was scanned to cover the full imaging field (Figure S1). For guide star generation, a single focal spot was shifted to excite fluorophore. For the 2P-MSIM imaging, varied multifocal arrays were adopted depending on different samples (Table S2).

### Data acquisition and wavefront correction

For all imaging, the detailed acquisition parameters were provided in Table S2. For all measurements, the electron multiplication gain of the EMCCD was set to 100–180. In external trigger mode, a small region of interest ( $512 \times 512$  pixels) was chosen. For wavefront correction, the image exposure on the SHS was set from 1.5 to 2 s, depending on the sample brightness. The control electronics and timing and the detailed processes of AO correction were described in the Supplemental information.

### Data processing and deconvolution

The theory of 2P-MSIM was described in the Supplemental information. Super-resolution 2P-MSIM images were obtained by postprocessing the raw images, which included pinholing the detected spots, magnifying the images while maintaining the size of the pinholed spots, integrating the scaled images over all positions, and deconvoluting the resulting image. The final super-resolution image has half the pixel size of the original raw images. We carried out the postprocessing mainly based on a freely available code from the website (<http://code.google.com/p/msim/>) [9]. The deconvolution was operated in ImageJ (Deconvolution lab, Richardson–Lucy deconvolution). The modeled point spread function of system was calculated as previously described [11], with numerical aperture (1.1), refractive index (1.33), and wavelength (1036 nm or 920 nm for excitation and 540 nm for emission).

### Preparation and staining of live zebrafish larvae

Zebrafish of Tg(mnx1:mGFP) and Tg(Xla.Eef1a1:mlsEGFP) were purchased from China Zebrafish Resource Center as eggs and raised in E3 solution (containing 0.003% N-phenylthiourea, Sigma) to inhibit pigmentation after 20 hpf. Before experiments, 2–5-dpf-old larvae were labeled with CellTracker Red CMTPX (1.1  $\mu\text{g}/\text{mL}$ , ThermoFisher Scientific, C34552) for 4 h at room temperature in the dark. After that, larvae were washed in E3 resolution twice for 10 min, anesthetized with 600  $\mu\text{M}$  Tricaine (Sigma, Cat. # E10521), and then mounted for imaging in 1% low-melting-point agarose (NuSieve GTG, Cat. # 50,080).

### Abbreviations

2P-MSIM	Two-photon multifocal structured illumination microscopy
AO	Adaptive optics
AO 2P-MSIM	Adaptive optical two-photon multifocal structured illumination microscopy
2PEM	Two-photon excitation microscopy
2P-ISIM	Two-photon instant structured illumination microscopy
ISM	image scanning microscopy
SNR	signal-to-noise ratio
DM	deformable mirror
SLM	Spatial light modulator
SHS	Shack–Hartmann wavefront sensor
EMCCD	electron multiplying charge-coupled device
MSIM	multifocal structured illumination microscopy
PSFs	Point spread functions
STED	Stimulated emission depletion microscopy
STORM	Stochastic optical reconstruction microscopy
PALM	Photo-activated localization microscopy
PBS	Polarizing beam splitter
WGS	Weighted Gerchberg-Saxton

### Supplementary Information

The online version contains supplementary material available at <https://doi.org/10.1186/s43074-023-00115-2>.

**Additional file 1: Figure S1.** Schematic diagram of multifocal structured illumination. Phase pattern (a) loaded onto the spatial light modulator (SLM) to generate a multifocal array (b) on the sample plane and the normalized intensity profile of foci in the rightmost column. The shift of focus arrays is controlled by adding a series of linear grating phases (c) on the SLM directly to cover the full field of view. Full illumination of sample plane (d) was obtained by scanning Eosin Y solution. Scale bar, 5  $\mu\text{m}$ . **Figure S2.** Evaluation of the performance of system correction using 1- $\mu\text{m}$ -diameter yellow-green fluorescent beads on a coverslip surface. (a) Images and corresponding intensity profiles of guide star without system correction (AO off), with only system correction in excitation path (Ex AO), with only system correction in emission path (Em AO), and with system correction in both excitation and emission paths

(Full AO). Scale bar, 1  $\mu\text{m}$ . (b) Wavefronts measured by Shack–Hartmann wavefront sensor (SHS) before (top) and after (bottom) system correction. (c) Top: Corrective phase pattern loaded onto SLM for system correction in the laser path. Bottom: Corrective deformable mirror (DM) voltages for system correction in the fluorescence path. **Figure S3.** Data processing in AO 2P-MSIM. Example datasets were obtained in a Thy1-YFP brain slice at 106- $\mu\text{m}$  depth. (a) A series of raw images were captured with system AO correction. A corresponding widefield (WF) image (Sys AO WF) was obtained by directly summing up the raw images. Pixel reassignment (PR) was conducted to enhance imaging resolution (Sys AO PR). The final super-resolution image (Sys AO MSIM) was obtained by further deconvolving (Dc). (b) The corresponding results with both system and sample AO correction (Full AO). (c) The intensity profiles of colorful lines in Sys AO PR, Sys AO MSIM, Full AO PR, and Full AO MSIM images. Scale bar, 5  $\mu\text{m}$  in large images and 2  $\mu\text{m}$  in detailed images. **Figure S4.** Comparison of deconvolution algorithms for resolution enhancement. The original WF and PR images from a Thy1-YFP brain slice were obtained by summing and pixel reassignment, respectively. The WF and PR images were further performed deconvolution by using Richardson–Lucy, Blind, and Wiener algorithms. Deconvolution of WF images resulted in limited resolution improvement than pixel reassignment alone. By having the aid of pixel reassignment in resolution improvement, the deconvolution algorithms visualized fine details of the sample. Scale bar, 5  $\mu\text{m}$  in large images and 2  $\mu\text{m}$  in detailed images. **Figure S5.** Estimation of the resolution of the AO 2P-MSIM system. (a) Exemplary images of a 100-nm-diameter yellow-green fluorescent bead on the coverslip surface after system correction, as viewed in lateral (top) and axial (bottom) cuts through the image stacks. From left to right: image with widefield resolution (sum of raw images), PR image (after pixel reassignment without deconvolution), MSIM image (after pixel reassignment and deconvolution). Scale bars, 0.5  $\mu\text{m}$ . (b) Intensity profiles through the center of each lateral and axial bead image. (c) Statistical comparison of lateral and axial resolution was derived from 32 beads. Means and standard deviations are shown. **Figure S6.** Spatial resolution assessment of the AO 2P-MSIM system at various depths. (a) The thick sample was prepared by mixing 100-nm-diameter fluorescent beads with 1- $\mu\text{m}$ -diameter fluorescent beads in 1% agarose. The big beads were considered guide stars because of their strong fluorescent signals and the nearby small beads were used to measure the resolution at different depths. (b) Lateral (top) and axial (bottom) images of representative 100-nm-diameter beads at different depths (100, 300, and 500  $\mu\text{m}$ ) show imaging results before/after correcting sample-induced aberrations and with further MSIM reconstruction. Scale bar, 0.5  $\mu\text{m}$ . (c) Averaged lateral and (d) axial resolution (31 beads) with/without correction for sample-induced aberrations and MSIM reconstruction at different depths. **Figure S7.** Average wavefronts before and after AO correction for sample-induced aberrations were detected at different depths within agarose (10, 100, 300, and 500  $\mu\text{m}$ ). **Figure S8.** Structural classification of the neuron from a Thy1-YFP brain slice. (a) Maximum intensity projection with color coding for depth of 12- $\mu\text{m}$ -thick image stacks after sample AO correction and MSIM reconstruction. Super-resolution imaging recognized the connection between soma (white dotted line), axon (magenta line 1), and dendrites (magenta lines 2 and 3). Cyan lines 4–7 represent dendrites from other somas. (b) The axon of soma in (a). (c–d) The dendrites of the soma in (a). (e–g) Dendrites from other somas. Scale bar, 2  $\mu\text{m}$ . **Figure S9.** In vivo AO 2P-MSIM imaging of motoneurons in *mnx1:mGFP* zebrafish. (a) The map of the imaging region was shown by the green square. (b) Images of Sys AO WF, Full AO WF, and Full AO MSIM. Scale bar, 2  $\mu\text{m}$ . **Figure S10.** In vivo AO 2P-MSIM imaging of motoneurons in anesthetized *mnx1:mGFP* zebrafish at increasing depths with an axial step size of 4  $\mu\text{m}$ . (a) The map of the imaging location was shown by the green square. (b) Images of Full AO WF and Full AO MSIM at depths from 24 to 332  $\mu\text{m}$ . As shown in the magnified views of the boxed region, the Full AO WF image was blurry because of obvious background noise and the Full AO MSIM image was high quality. The corresponding intensity profiles of dotted lines are indicated by purple line (WF) and orange line (MSIM). Scale bar, 5  $\mu\text{m}$  in large images and 2  $\mu\text{m}$  in detailed images. **Figure S11.** In vivo AO 2P-MSIM imaging of mitochondrion in anesthetized *Xla.Eef1a1:mEGFP* zebrafish at 300 depth with an axial step size of 0.2  $\mu\text{m}$ . (a) Lateral (top) and axial (bottom) images of Sys AO WF, Full AO WF, and Full AO MSIM show the enhancement of resolution by AO correction and MSIM processing. Scale bar, 5  $\mu\text{m}$ . (b) The intensity profiles of dotted lines show the enhancement of lateral resolution. (c) The intensity profiles of the structures indicated by asterisks show the improvement of axial resolution. **Figure S12.** Sequence control operation of 2P-MSIM scanning. (a) Multifocal arrays traverse the entire field of view according to raster-scanning. (b) Time sequence of the synchronization of the SLM and EMCCD at the same rate. Top: the series pattern loaded onto the SLM; Bottom: the EMCCD that operates under a synchronous trigger mode. (c) Time sequence of the synchronization of the SLM and EMCCD at different rates. Top: the series pattern loaded onto the SLM at an  $n$ -fold rate than EMCCD; Bottom: the EMCCD that operates under a multiplexing trigger mode. During a single exposure time of the EMCCD,  $n$  phase patterns are loaded onto the SLM in turn. (d) In synchronous trigger mode,  $m$  raw images are captured according to phase patterns loaded onto the SLM. (e) In multiplexing trigger mode, the EMCCD only captures  $m/n$  raw images. The distance between adjacent focus points in the fluorescent image becomes closer, leading to some SNR reduction. **Figure S13.** Eosin Y dissolved in 1% agarose was imaged with various EMCCD and SLM rates. (a) Eosin Y was scanned in 20, 40, 60, and 80 Hz with SLM while images were captured with EMCCD at the same rate. The corresponding intensity profiles (bottom) of foci are indicated by white lines (top). (b) Images were captured with EMCCD at 90 Hz while the sample was scanned at 90 and 360 Hz, respectively. (c) The sample was scanned at 100 Hz while images were captured at 25 and 100 Hz, respectively. Scale bar, 4  $\mu\text{m}$ . **Figure S14.** The flowchart of a phase pattern generation for focus arrays. **Figure S15.** Aberration compensation of AO 2P-MSIM. (a) Left: Spot pattern detected by SHS before AO correction. Middle: Corresponding higher magnification views of the boxed region. Right: Reconstructed wavefront using a zonal approach. (b) Corrective voltages of the DM. (c) Corrective phase pattern loaded on the SLM. (d) Left: Spot pattern detected by the SHS after AO correction. Middle: Corresponding higher magnification views of the boxed region. Right: Reconstructed wavefront. **Table S1.** Adaptive recovery of resolution at progressively increasing distances from the coverslip (aberrations increase with distance). **Table S2.** Acquisition parameters used in this work.

### Authors' contributions

J.Q., B.Y., and D.L. conceived and supervised the project. C.Z., B.Y., and J.Q. designed the optical system. C.Z. built the AO 2P-MSIM system and developed the hardware control program. F.L. performed the mouse brain surgery and K.S. and W.G. provided support for its operation. H.Y. and W.Z. built MSIM setup and provided support on multifocal arrays generation. C.S. supervised zebrafish experiments. Y.J. supervised beads experiments. C.Z. analyzed data and prepared all figures and supplementary material. C.Z., D.L. and S.S. wrote the manuscript with feedback from J.Q., B.Y., and all other authors.

### Funding

This work has been partially supported by the National Key R&D Program of China (2021YFF0502900), National Natural Science Foundation of China (61975131, 62175166, and 62127819), Shenzhen Key Laboratory of Photonics and Biophotonics (ZDSYS20210623092006020) and Shenzhen Science and Technology Program (JCYJ20220818100202005, JCYJ20200109105411133).

### Availability of data and materials

All relevant data are available from the corresponding authors upon reasonable request.

### Declarations

#### Ethics approval and consent to participate

This project complied with all relevant ethical regulations for animal testing and research. All experimental procedures were conducted with ethical approval from the Animal Care and Use Committee of Shenzhen University.

#### Competing interests

The authors declare that they have no competing interests.

Received: 27 July 2023 Revised: 8 November 2023 Accepted: 27 November 2023

Published online: 21 December 2023

### References

1. Al-Hasani R, Gowrishankar R, Schmitz GP, Pedersen CE, Marcus DJ, Shirley SE, et al. Ventral tegmental area GABAergic inhibition of cholinergic interneurons in the ventral nucleus accumbens shell promotes reward reinforcement. *Nat Neurosci*. 2021;24(10):1414–28.
2. Yuste R, Denk W. Dendritic spines as basic functional units of neuronal integration. *Nature*. 1995;375(6355):682–4.
3. Nimchinsky EA, Sabatini BL, Svoboda K. Structure and function of dendritic spines. *Annu Rev Physiol*. 2002;64:313–53.
4. Ji N, Shroff H, Zhong H, Betzig E. Advances in the speed and resolution of light microscopy. *Curr Opin Neurobiol*. 2008;18(6):605–16.
5. Turcotte R, Liang Y, Tanimoto M, Zhang Q, Li Z, Koyama M, et al. Dynamic super-resolution structured illumination imaging in the living brain. *Proc Natl Acad Sci U S A*. 2019;116(19):9586–91.
6. Gribble KD, Walker LJ, Saint-Amant L, Kuwada JY, Granato M. The synaptic receptor Lrp4 promotes peripheral nerve regeneration. *Nat Commun*. 2018;9(1):2389.
7. Denk W, Strickler JH, Webb WW. Two-photon laser scanning fluorescence microscopy. *Science*. 1990;248(4951):73–6.
8. Helmchen F, Denk W. Deep tissue two-photon microscopy. *Nat Methods*. 2005;2(12):932–40.
9. Ingaramo M, York AG, Wawrzusin P, Milberg O, Hong A, Weigert R, et al. Two-photon excitation improves multifocal structured illumination microscopy in thick scattering tissue. *Proc Natl Acad Sci U S A*. 2014;111(14):5254–9.
10. Winter PW, York AG, Nogare DD, Ingaramo M, Christensen R, Chitnis A, et al. Two-photon instant structured illumination microscopy improves the depth penetration of super-resolution imaging in thick scattering samples. *Optica*. 2014;1(3):181–91.
11. Zheng W, Wu Y, Winter P, Fischer R, Nogare DD, Hong A, et al. Adaptive optics improves multiphoton super-resolution imaging. *Nat Methods*. 2017;14(9):869–72.
12. Muller CB, Enderlein J. Image scanning microscopy. *Phys Rev Lett*. 2010;104(19):198101.
13. Sheppard CJ, Mehta SB, Heintzmann R. Superresolution by image scanning microscopy using pixel reassignment. *Opt Lett*. 2013;38(15):2889–92.
14. Ji N, Milkie DE, Betzig E. Adaptive optics via pupil segmentation for high-resolution imaging in biological tissues. *Nat Methods*. 2010;7(2):141–7.
15. Sahu P, Mazumder N. Advances in adaptive optics-based two-photon fluorescence microscopy for brain imaging. *Lasers Med Sci*. 2020;35(2):317–28.
16. Ji N, Freeman J, Smith SL. Technologies for imaging neural activity in large volumes. *Nat Neurosci*. 2016;19(9):1154–64.
17. Booth M. Adaptive optical microscopy: the ongoing quest for a perfect image. *Light Sci Appl*. 2014;3(4):e165–165.
18. Zhou Z, Huang J, Li X, Gao X, Chen Z, Jiao Z, et al. Adaptive optical microscopy via virtual-imaging-assisted wavefront sensing for high-resolution tissue imaging. *Photonix*. 2022;3(1):1–20.
19. Shu Y, Sun J, Lyu J, Fan Y, Zhou N, Ye R, et al. Adaptive optical quantitative phase imaging based on annular illumination Fourier ptychographic microscopy. *Photonix*. 2022;3(1):24.
20. Wu J, Lu Z, Jiang D, Guo Y, Qiao H, Zhang Y, et al. Iterative tomography with digital adaptive optics permits hour-long intravital observation of 3D subcellular dynamics at millisecond scale. *Cell*. 2021;184(12):3318–32e17.

21. Tao X, Norton A, Kissel M, Azucena O, Kubby J. Adaptive optical two-photon microscopy using autofluorescent guide stars. *Opt Lett*. 2013;38(23):5075–8.
22. Wang K, Milkie DE, Saxena A, Engerer P, Misgeld T, Bronner ME, et al. Rapid adaptive optical recovery of optimal resolution over large volumes. *Nat Methods*. 2014;11(6):625–8.
23. Wang K, Sun W, Richie CT, Harvey BK, Betzig E, Ji N. Direct wavefront sensing for high-resolution in vivo imaging in scattering tissue. *Nat Commun*. 2015;6:7276.
24. Kashiwagi Y, Higashi T, Obashi K, Sato Y, Komiyama NH, Grant SGN, et al. Computational geometry analysis of dendritic spines by structured illumination microscopy. *Nat Commun*. 2019;10(1):1285.
25. Ke M-T, Nakai Y, Fujimoto S, Takayama R, Yoshida S, Kitajima Tomoya S, et al. Super-resolution Mapping of neuronal circuitry with an Index-Optimized Clearing Agent. *Cell Rep*. 2016;14(11):2718–32.
26. Balcioglu A, Gillani R, Doron M, Burnell K, Ku T, Erisir A, et al. Mapping thalamic innervation to individual L2/3 pyramidal neurons and modeling their 'readout' of visual input. *Nat Neurosci*. 2023;26(3):470–80.
27. Ruthazer ES, Li J, Cline HT. Stabilization of axon branch dynamics by synaptic maturation. *J Neurosci*. 2006;26(13):3594–603.
28. Niell CM, Meyer MP, Smith SJ. In vivo imaging of synapse formation on a growing dendritic arbor. *Nat Neurosci*. 2004;7(3):254–60.
29. Huang B, Li J, Yao B, Yang Z, Lam EY, Zhang J, et al. Enhancing image resolution of confocal fluorescence microscopy with deep learning. *Photonix*. 2023;4(1):1–22.
30. Liao J, Zhang C, Xu X, Zhou L, Yu B, Lin D, et al. Deep-MSIM: fast image reconstruction with deep learning in multifocal structured illumination microscopy. *Adv Sci*. 2023;10(27):2300947.
31. Kim D, Keesling A, Omran A, Levine H, Bernien H, Greiner M, et al. Large-scale uniform optical focus array generation with a phase spatial light modulator. *Opt Lett*. 2019;44(12):3178–81.

### Publisher's Note

Springer Nature remains neutral with regard to jurisdictional claims in published maps and institutional affiliations.

**Submit your manuscript to a SpringerOpen<sup>®</sup> journal and benefit from:**

- ▶ Convenient online submission
- ▶ Rigorous peer review
- ▶ Open access: articles freely available online
- ▶ High visibility within the field
- ▶ Retaining the copyright to your article

---

Submit your next manuscript at ▶ [springeropen.com](https://www.springeropen.com)

---